Asymptotic expansion homogenization for multiscale nuclear fuel analysis

CrossMark

J.D. Hales [a,*], M.R. Tonks [a], K. Chockalingam [b], D.M. Perez [a], S.R. Novascone [a], B.W. Spencer [a], R.L. Williamson [a]

[a] Fuel Modeling and Simulation, Idaho National Laboratory, P.O. Box 1625, Idaho Falls, ID 83415-3840, United States
[b] Interdisciplinary Centre for Advanced Materials Simulation, Ruhr-Universität Bochum, Universitätsstraße 150, 44801 Bochum, Germany

ARTICLE INFO

ABSTRACT

Engineering scale nuclear fuel performance simulations can benefit by utilizing high-fidelity models running at a lower length scale. Lower length-scale models provide a detailed view of the material behavior that is used to determine the average material response at the macroscale. These lower length-scale calculations may provide insight into material behavior where experimental data is sparse or nonexistent.

This multiscale approach is especially useful in the nuclear field, since irradiation experiments are difficult and expensive to conduct. The lower length-scale models complement the experiments by influencing the types of experiments required and by reducing the total number of experiments needed. This multiscale modeling approach is a central motivation in the development of the BISON and MARMOT fuel performance codes. These codes seek to provide more accurate and predictive solutions for nuclear fuel behavior.

One critical aspect of multiscale modeling is the ability to extract the relevant information from the lower length-scale simulations. One approach, the asymptotic expansion homogenization (AEH) technique, has proven to be an effective method for determining homogenized material parameters. The AEH technique prescribes a system of equations to solve at the mesoscale that are used to compute homogenized material constants for use at the engineering scale.

In this work, we employ AEH to explore the effect of evolving microstructural thermal conductivity and elastic constants on nuclear fuel performance. We show that the AEH approach fits cleanly into the BISON and MARMOT codes and provides a natural, multidimensional homogenization capability.

© 2015 Elsevier B.V. All rights reserved.

1. Introduction

In UO_2 fuel for light water reactors, the radiation environment causes defect generation and microstructure evolution. This evolution affects the properties of the fuel, including thermal conductivity, swelling, densification, creep, and fission gas production and release. However, engineering scale modeling typically employs empirical models that follow the observable trends from experimental data. As an example, the Fink-Lucuta model of thermal conductivity [1,2] is a function of temperature and burnup.

Conducting experiments on irradiated nuclear fuel materials provides essential, fundamental data for understanding the behavior of fuel, cladding, and other components. This data may be analyzed in an effort to create or improve an empirical engineering scale model. These experiments are, however, difficult and expensive to perform due to the inherent radioactivity of the system.

Computational experiments have many advantages. Through computer modeling, geometries, initial conditions, boundary conditions, and material models can be analyzed relatively quickly and inexpensively. It is also possible to feed numerical solutions from lower length-scale analyses to engineering scale calculations. Macroscale analyses can thus be informed with mesoscale information. In this way, changes in the fuel properties can be represented in terms of the microstructure evolution.

With a validated approach to conducting computational experiments, it may be possible to reduce the number of necessary physical experiments. This can be accomplished, for example, by employing computational techniques to eliminate less-promising candidates in a suite of material tests.

When modeling at the mesoscale, it is not sufficient to determine the evolution of the microstructure. It is also necessary to

---

* Corresponding author.
E-mail addresses: Jason.Hales@inl.gov (J.D. Hales), Michael.Tonks@inl.gov (M.R. Tonks), karthikeyan.chockalingam@rub.de (K. Chockalingam), Danielle.Perez@inl.gov (D.M. Perez), Stephen.Novascone@inl.gov (S.R. Novascone), Benjamin.Spencer@inl.gov (B.W. Spencer), Richard.Williamson@inl.gov (R.L. Williamson).

determine the effective material properties of the new microstructure. One approach to calculating effective properties is asymptotic expansion homogenization (AEH) [3–7]. Based on the finite element method, AEH is a computational technique that can seamlessly couple the macro- and microscale together by passing a homogenized property to the engineering scale. As mentioned, the microstructure is constantly evolving and, hence, so are the macroscale properties. In the current work, AEH is used with the phase field method [8], which captures the evolving characteristics of the microscale structure. Thereby, AEH concurrently computes the thermal conductivity (or other properties) of this complex system as the simulation progresses.

Many other approaches to calculating effective material properties exist. Perhaps the most straightforward approach is a volume weighted average. In this approach, we seek an effective property p_e based on the volume fraction f_i and the property p_i of the ith constituent. Then, $p_e = \sum f_i p_i$. Comparisons of results from the AEH approach and the volume weighted average approach (known as the rule of mixtures for long fiber composites) will be made. See [9] for a survey of approaches for solid mechanics problems. For a comprehensive review of multiscale methods, see [10].

The fuel simulation codes BISON [11] and MARMOT [12], under development at Idaho National Laboratory, have been built with a vision of multiphysics/multiscale modeling in mind. Both codes are built on the MOOSE framework [13], which is a general partial differential equation (PDE) solver. MOOSE solves PDEs using the finite element method with implicit time integration. The equations are solved fully-coupled using the Jacobian-free Newton–Krylov [14] method. They run efficiently on parallel computers.

BISON is a multidimensional nuclear fuel performance analysis code capable of 1D, 2D, and 3D simulations. It is applicable to engineering scale analysis of LWR fuel, TRISO-coated fuel particles [15], and metal fuels [16,17]. Typically, the PDEs that BISON solves are the energy and solid mechanics equations for temperature and displacements, respectively. BISON's capabilities include a selection of fuel and cladding thermal and mechanical material models, fission gas release, thermal and mechanical contact, evolving gap conductivity and pressure, axial and radial power scaling, fuel densification and swelling, and other models. Due to the evolution of gap size between fuel and cladding in a light water reactor, solving the energy and mechanics equations in a fully-coupled manner is very important. It is also possible to run BISON coupled with a neutronics code [18].

MARMOT is a multiphysics mesoscale simulation code focused on modeling the co-evolution of microstructure and material properties. In MARMOT, the system of phase field PDEs is solved simultaneously with PDEs defining additional physics such as heat conduction and solid mechanics. MARMOT takes advantage of advanced tools such as automatic mesh and time step adaptivity. MARMOT has been used to model various microstructural phenomena, ranging from grain boundary migration to bubble growth and coalescence.

When BISON and MARMOT are run together, they are typically coupled via temperature calculations in BISON and corresponding thermal conductivity calculations in MARMOT.

The paper proceeds with a review of the derivation of the pertinent equations for AEH, followed by a discussion on application of AEH to heat conduction and solid mechanics. Next is a section reviewing solutions to standard benchmark problems from the literature. That is followed by a discussion of mesh convergence. The next section presents results on homogenizing elastic constants and thermal conductivity applicable to nuclear fuel simulation, including application to cladding and UO_2. Next is a demonstration of the technique applied to a simple but complete UO_2/cladding model. The final section gives conclusions and a discussion of future work.

2. Derivation

We now show the derivation of the asymptotic expansion homogenization equations (see [19]). Consider a domain where the material at the mesoscale may be represented as a periodic structure. A quantity of interest at the macroscale, u^e, incorporates macroscale (x) and mesoscale (y) information. We may choose to model a particular material behavior with the following partial differential equation:

$$\frac{\partial}{\partial x_i^e}\left(a_{ij}\frac{\partial}{\partial x_j^e}\right)u^e = f \tag{1}$$

with appropriate boundary conditions. Given that the solution u^e incorporates macroscale and mesoscale information, $u^e = f(x^e) = f(x,y)$. If the relationship between the actual size of characteristic lengths between the macroscale and mesoscale is given as $\epsilon = x/y$, the following holds:

$$\frac{\partial}{\partial x_i^e} = \frac{\partial}{\partial x_i} + \frac{\partial}{\partial y_i}\frac{\partial y_i}{\partial x_i}$$
$$\frac{\partial}{\partial x_i^e} = \frac{\partial}{\partial x_i} + \frac{1}{\epsilon}\frac{\partial}{\partial y_i}. \tag{2}$$

We represent u^e with an asymptotic series:

$$u^e = u^{(0)}(x,y) + \epsilon u^{(1)}(x,y) + \epsilon^2 u^{(2)}(x,y) + \ldots \tag{3}$$

Combining Eqs. (1)–(3), we obtain

$$\left(\frac{\partial}{\partial x_i} + \frac{1}{\epsilon}\frac{\partial}{\partial y_i}\right)\left[a_{ij}\left(\frac{1}{\epsilon}\frac{\partial u^{(0)}}{\partial y_j} + \left[\frac{\partial u^{(0)}}{\partial x_j} + \frac{\partial u^{(1)}}{\partial y_j}\right] + \epsilon\left[\frac{\partial u^{(1)}}{\partial x_j} + \frac{\partial u^{(2)}}{\partial y_j}\right] + \epsilon^2\frac{\partial u^{(2)}}{\partial x_j} + \ldots\right)\right]$$
$$= f. \tag{4}$$

This is expanded to

$$\epsilon^{-2}\left[\frac{\partial}{\partial y_i}\left(a_{ij}\frac{\partial u^{(0)}}{\partial y_j}\right)\right]$$
$$+ \epsilon^{-1}\left[\frac{\partial}{\partial x_i}\left(a_{ij}\frac{\partial u^{(0)}}{\partial y_j}\right) + \frac{\partial}{\partial y_i}\left(a_{ij}\left(\frac{\partial u^{(0)}}{\partial x_j} + \frac{\partial u^{(1)}}{\partial y_j}\right)\right)\right]$$
$$+ \epsilon^0\left[\frac{\partial}{\partial x_i}\left(a_{ij}\left(\frac{\partial u^{(0)}}{\partial x_j} + \frac{\partial u^{(1)}}{\partial y_j}\right)\right) + \frac{\partial}{\partial y_i}\left(a_{ij}\left(\frac{\partial u^{(1)}}{\partial x_j} + \frac{\partial u^{(2)}}{\partial y_j}\right)\right)\right]$$
$$+ \epsilon^1[\ldots] + \epsilon^2[\ldots] + \ldots$$
$$= f. \tag{5}$$

As will be shown, only the ϵ^{-2}, ϵ^{-1}, and ϵ^0 terms are needed to develop the homogenization equations.

For this equation to hold for arbitrarily small ϵ, each portion of the equation associated with a particular power of ϵ must be equal to zero. Thus,

$$\frac{\partial}{\partial y_i}\left(a_{ij}\frac{\partial u^{(0)}}{\partial y_j}\right) = 0. \tag{6}$$

For this to be true, $u^{(0)}$ must not be dependent on y. Therefore, $u^{(0)}$ is the solution at the macroscale.

Now, let us define the average of a function $\phi(y)$ over the periodic domain Y as $\bar{\phi}$:

$$\bar{\phi} = \frac{1}{|Y|}\int_Y \phi(y)\,\mathrm{d}y. \tag{7}$$

The resulting $\bar{\phi}$ is not a function of y.

Continuing with the ϵ^0 term,

$$\frac{\partial}{\partial x_i}\left(a_{ij}\left(\frac{\partial u^{(0)}}{\partial x_j} + \frac{\partial u^{(1)}}{\partial y_j}\right)\right) + \frac{\partial}{\partial y_i}\left(a_{ij}\left(\frac{\partial u^{(1)}}{\partial x_j} + \frac{\partial u^{(2)}}{\partial y_j}\right)\right) = f. \tag{8}$$

For convenience, let A represent the first and B the second term of the above equation. Using Eq. (7),

$$\bar{B} = \frac{1}{|Y|} \int_Y B \, dy = \frac{1}{|Y|} \int_{\partial Y} n \, a_{ij} \left(\frac{\partial u^{(1)}}{\partial x_j} + \frac{\partial u^{(2)}}{\partial y_j} \right) dy \tag{9}$$

where the second form comes via the divergence theorem. Given that $u^{(1)}$ and $u^{(2)}$ are periodic on Y, they have equal values on opposite sides of the domain. Since the normal n points in opposite directions on opposite sides of the domain, $\bar{B} = 0$. This gives

$$\bar{A} = \bar{f} \tag{10}$$

and

$$\frac{1}{|Y|} \int_Y \frac{\partial}{\partial x_i} \left(a_{ij} \left(\frac{\partial u^{(0)}}{\partial x_j} + \frac{\partial u^{(1)}}{\partial y_j} \right) \right) dy = \bar{f} = f. \tag{11}$$

Recalling Eq. (7), it can be seen that $\bar{f} = f$ as long as f is a function of x but not a function of y.

Now turning to the ϵ^{-1} term of Eq. (5) (recall that $u^{(0)}$ is not a function of y),

$$-\frac{\partial}{\partial y_i} \left(a_{ij} \frac{\partial u^{(1)}}{\partial y_j} \right) = \frac{\partial a_{ij}}{\partial y_i} \frac{\partial u^{(0)}}{\partial x_j}. \tag{12}$$

Multiplying by a test function v and integrating over the domain, we obtain

$$-\int_Y \frac{\partial}{\partial y_i} \left(a_{ij} \frac{\partial u^{(1)}}{\partial y_j} \right) v \, dy = \int_Y \frac{\partial a_{ij}}{\partial y_i} \frac{\partial u^{(0)}}{\partial x_j} v \, dy. \tag{13}$$

This leads to

$$-\int_{\partial Y} n \, a_{ij} \frac{\partial u^{(1)}}{\partial y_j} \, v \, dy + \int_Y \frac{\partial v}{\partial y_i} a_{ij} \frac{\partial u^{(1)}}{\partial y_j} \, dy = \int_Y \frac{\partial a_{ij}}{\partial y_i} \frac{\partial u^{(0)}}{\partial x_j} v \, dy. \tag{14}$$

The first term in the above equation is equal to zero due to its periodic nature.

Let

$$u^{(1)} = \chi^j(y) \partial u^{(0)}/\partial x_j + C(x). \tag{15}$$

Then

$$\int_Y \frac{\partial v}{\partial y_i} a_{ij} \frac{\partial \chi^k}{\partial y_j} \frac{\partial u^{(0)}}{\partial x_k} \, dy = \int_Y \frac{\partial a_{ij}}{\partial y_i} \frac{\partial u^{(0)}}{\partial x_j} v \, dy, \tag{16}$$

which allows

$$\int_Y \frac{\partial v}{\partial y_i} a_{ij} \frac{\partial \chi^k}{\partial y_j} \, dy = \int_Y \frac{\partial a_{ik}}{\partial y_i} v \, dy = \int_{\partial Y} n \, a_{ik} v \, dy - \int_Y \frac{\partial v}{\partial y_i} a_{ik} \, dy = -\int_Y \frac{\partial v}{\partial y_i} a_{ik} \, dy. \tag{17}$$

We have taken advantage of the fact that $\partial u^{(0)}/\partial x$ appears on both sides of Eq. (16) and may be eliminated. We have also eliminated, as we have previously, a term integrated over the boundary of Y due to the periodic nature of the mesoscale domain. From Eqs. (11) and (15)

$$a_{ij} \left(\frac{\partial u^{(0)}}{\partial x_j} + \frac{\partial u^{(1)}}{\partial y_j} \right) = a_{ij} \left(\frac{\partial u^{(0)}}{\partial x_j} + \frac{\partial \chi^k}{\partial y_j} \frac{\partial u^{(0)}}{\partial x_k} \right) = \left(a_{ij} + a_{ij} \frac{\partial \chi^k}{\partial y_j} \right) \frac{\partial u^{(0)}}{\partial x_k}. \tag{18}$$

Substituting this result into Eq. (11),

$$\frac{\partial}{\partial x_i} \frac{1}{|Y|} \int_Y \left(a_{ij} + a_{ij} \frac{\partial \chi^k}{\partial y_j} \right) dy \frac{\partial u^{(0)}}{\partial x_k} = f. \tag{19}$$

Let

$$a_{ij}^H = \frac{1}{|Y|} \int_Y \left(a_{ij} + a_{ij} \frac{\partial \chi^k}{\partial y_j} \right) dy. \tag{20}$$

Then, Eq. (20) becomes

$$\frac{\partial}{\partial x_i} a_{ij}^H \frac{\partial u^{(0)}}{\partial x_j} = f, \tag{21}$$

which is the expression for the macroscale solution $u^{(0)}$ using homogenized properties a_{ij}^H.

3. Application

Given the similarity between the PDE in Eq. (1) and the PDE for heat conduction, the system to be solved on the mesoscale in the case of heat conduction is (see Eq. (17)

$$\int_Y \frac{\partial v}{\partial y_i} k_{ij} \frac{\partial \psi^k}{\partial y_j} dy = \int_Y \frac{\partial v}{\partial y_i} k_{ik} dy \; \forall v_i \in V_Y \tag{22}$$

with spatially-dependent k_{ij} and periodic boundary conditions. With ψ^k known, the homogenized, anisotropic thermal conductivity k_{ij}^H is computed as (see Eq. (20))

$$k_{ij}^H = \frac{1}{|Y|} \int_Y k_{ij} \left(I + \frac{\partial \psi^k}{\partial y_j} \right) dy. \tag{23}$$

The heat conduction equations may then be solved at the macroscale using k_{ij}^H as the thermal conductivity. Problem details occurring only at the macroscale (volumetric heat sources and boundary conditions, for example) require no special treatment. Therefore, once the homogenized material properties are computed, using them requires trivial if any changes to existing software.

It is noted that the microstructure under consideration is assumed to have the same temperature at every point. It is conventional to make such an approximation provided the thermal gradient is not steep. In the case of steep thermal gradients, nonlinear AEH methods [20] are employed, and the temperature need not be assumed to be the same at every point in the microstructure. However, [20] states that linear methods are generally sufficient.

The auxiliary system of equations for elasticity is

$$\int_Y \frac{\partial v_i}{\partial y_j} D_{ijkl} \frac{\partial \chi_\kappa^{mn}}{\partial y_l} dy = \int_Y \frac{\partial v_i}{\partial y_j} D_{ijkl} \, dy \; \forall v_i \in V_Y. \tag{24}$$

The homogenized, anisotropic elasticity constants are determined by

$$D_{ijkl}^H = \frac{1}{|Y|} \int_Y D_{ijkl} \left(I + \frac{\partial \chi_\kappa^{mn}}{\partial y_l} \right) dy. \tag{25}$$

In matrix notation for the finite element method, and with the subscript n representing degrees of freedom and e indicating a given element, the equations for homogenization of thermal conductivity are

$$\int_Y [B_{in}]^T [K_{ij}][B_{jn}] \, dy [\psi_{nk}] = \int_Y [B_{in}]^T [K_{ik}] \, dy \tag{26}$$

and

$$[K_{ij}^h] = \sum^{nelem} \frac{V^e}{V^{tot}} [K_{il}^e] \left([I_{lk}] + [B_{ln}^e][\psi_{nk}^e] \right). \tag{27}$$

For solid mechanics, the symmetry of the elasticity, stress, and strain tensors allows the three dimensional elasticity tensor to be represented as a 6×6 matrix and the stress and strain tensors to be represented by 6×1 vectors. Using this convention with Greek subscripts using a range of 1–6, the matrix equations are

$$\int_Y [B_{\alpha n}]^T [D_{\alpha \beta}][B_{\beta n}] \, dy [\chi_{n\kappa}] = \int_Y [B_{\alpha n}]^T [D_{\alpha \kappa}] \, dy \tag{28}$$

and

$$[D_{\alpha \kappa}^H] = \sum^{nelem} \frac{V^e}{V^{tot}} [D_{\alpha \beta}^e] \left([I_{\beta \kappa}] + [B_{\beta n}^e][\chi_{n\kappa}^e] \right). \tag{29}$$

A key point to understand is the fact that the RHS of Eq. (26) and (28) is not a vector but a matrix. Each column of the RHS matrix corresponds to a column of the constitutive matrix $[K]$ or $[D]$. Thus, the solutions $[\psi]$ and $[\chi]$ are sets of solution vectors. In three dimensions, the $[\psi]$ matrix has three columns, and the $[\chi]$ matrix has six columns.

Once the macro scale solution is known, it is possible to recover the mesoscale response. The equations are not given here, but [21] gives details of the approach.

One may also compute homogenized thermal expansion coefficients and other homogenized parameters. A different derivation is required for the homogenization of new properties. However, the overall procedure is the same. A recipe for deriving the necessary equations is given in [21].

4. Standard benchmark problem results

To verify that the implementation of this technique is correct, the results obtained using BISON and MARMOT are compared to solutions of standard problems. For heat conduction, consider a simple unit cube domain divided equally along the x-axis into halves. One half has a thermal conductivity of 10 and the other half has a thermal conductivity of 100. The analytic solution for the homogenized thermal conductivity in the x direction is found by summing the thermal resistance, recognizing that the halves are in series.

$$R_x = \frac{L}{Ak_x} = R_1 + R_2 = \frac{L_1}{A_1 k_1} + \frac{L_2}{A_2 k_2} = \frac{0.5}{1 \cdot 10} + \frac{0.5}{1 \cdot 100} = 0.055$$

where R is resistance, L is length, A is area, and the subscripts represent each of the two materials. Since in this case the length and area have a magnitude of one, $k_x = 18.1818 \, (1/R_x)$.

The analytic solution for the homogenized thermal conductivity in the y direction is found similarly, with the recognition that the halves are in parallel.

$$\frac{1}{R_y} = \frac{Ak_y}{L} = \frac{1}{R_1} + \frac{1}{R_2} = \frac{0.5 \cdot 10}{1} + \frac{0.5 \cdot 100}{1} = 55.0$$

Thus, $k_y = 55.0$.

BISON/MARMOT compute these analytic solutions exactly using the AEH approach.

For an elasticity demonstration, we consider the so-called short fiber and long fiber problems defined in [4]. These problems involve square, periodic domains containing fiber and matrix materials. The geometry for these problems is shown in Fig. (1). The fiber portion of the problem is defined with a Young's modulus of 400 GPa and a Poisson's ratio of 0.2. The matrix portion is defined with a Young's modulus of 72.5 GPa and a Poisson's ratio of 0.33.
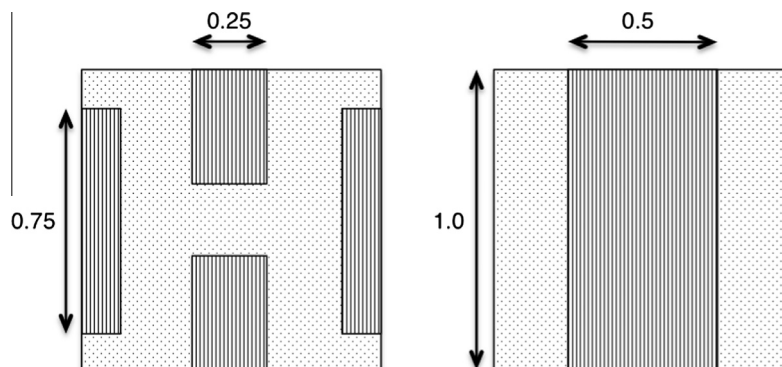
The AEH technique was used in BISON/MARMOT to compute the four unique homogenized elasticity tensor entries (1111, 2222, 1212, and 1122) for these problems. The four values were obtained using Eq. (25), and the four solution vectors in χ computed from Eq. (24). The results are compared to data from other computations given in [4] that are considered in that reference to be trusted solutions. See Table 1 for the short fiber problem results and Table 2 for the long fiber problem results. The results obtained by BISON/MARMOT match the reported data very well.

5. Mesh Convergence

Finite element solutions are more accurate with finer meshes, and this characteristic applies to AEH simulations. However, the method does not inherently require very fine meshes for accurate solutions. To demonstrate, consider the matrix and fiber model shown in Fig. 2. This model was run with increasingly fine meshes to show how the elasticity constants change with mesh refinement. The material properties for the matrix and fiber constituents are the same as for the short and long fiber problems of the previous section. As with all AEH simulations, periodic boundary conditions are applied on opposite faces.

As can be seen in Fig. 3, the elasticity constants vary little as the mesh is refined beyond the level where it contains about 1000

Table 1
Homogenized elasticity constants for the short fiber problem calculated by BISON/MARMOT, shown with results from [4] in the second and third columns for comparison. BISON/MARMOT results are very close to the HOMO2D and Fish and Wagiman solutions.
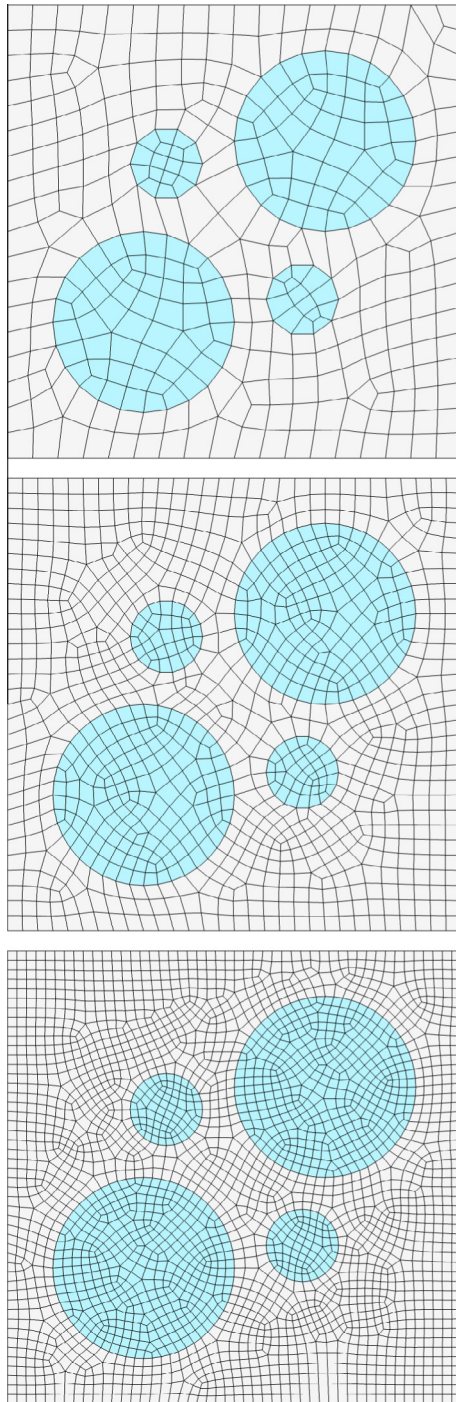
	BISON/MARMOT	HOMO2D	Fish and Wagiman
E1111 (GPa)	122.457	122.4	122.457
E2222 (GPa)	151.351	151.2	151.351
E1212 (GPa)	42.112	42.10	42.112
E1122 (GPa)	36.191	36.23	36.191

Table 2
Homogenized elasticity constants for the long fiber problem calculated by BISON/MARMOT, shown with results from [4] in the second and third columns for comparison. BISON/MARMOT results are very close to the HOMO2D and Fish and Wagiman solutions.

	BISON/MARMOT	HOMO2D	Fish and Wagiman
E1111 (GPa)	136.138	136.1	136.147
E2222 (GPa)	245.810	245.8	245.81
E1212 (GPa)	46.8498	46.85	46.85
E1122 (GPa)	36.076	36.08	36.076

Fig. 1. Short fiber (left) and long fiber (right) geometries. Dark areas are fibers, light areas are matrix. Figure reproduced from [4].

Fig. 2. Lower scale meshes used in the mesh convergence study with 398, 1092, and 2697 nodes.

Fig. 3. Elasticity constants with mesh refinement. The constants vary little when the mesh contains more than ∼1000 nodes.

nodes. It is also worth noting that due to the symmetry of this example, we would expect the E1111 and E2222 constants to be equal. At about 1000 nodes, these quantities match. This simple demonstration shows that the AEH technique can provide useful data without overly fine meshes and large computational expense.

6. Application to nuclear fuel simulations

6.1. Hydrides in cladding

The effect of hydrides in cladding is an important concern for cladding integrity both in-reactor and during long term storage of used nuclear fuel. In particular, an increasing hydride concentration reduces the ductility of the cladding. Furthermore, the cladding becomes more susceptible to cracking as hydrides reorient from a circumferential arrangement to a radial one during storage [22].

Given the expense of testing irradiated cladding specimens with hydride inclusions, it is attractive to consider numerical tools that may provide insight into cladding/hydride behavior. For example, [23] have developed a constitutive model for damage of Zircaloy containing circumferential and radial hydrides. The goal of that model is to provide a means to predict cladding failure.

In contrast to that advanced approach, the AEH technique provides a simple and inexpensive way of understanding inhomogeneous material such as cladding with hydrides. The example shown here is not meant to be representative of an actual cladding specimen, but it does show that the AEH procedure can give insight beyond simple assumptions and has the potential to give much more accurate and predictive data.

We take as our model a cladding/hydride composite where the hydrides are modeled as idealized inclusions in the model. For simplicity, we use the short fiber model geometry from Section 4. The material constants for the matrix are: Young's modulus, 75 GPa; Poisson's ratio, 0.3. The material constants for the inclusions are: Young's modulus, 140 GPa; Poisson's ratio, 0.27. The model is analyzed in plane stress conditions.

The size of the inclusions was varied such that a scaling parameter of 0 would indicate no inclusion, 1 would result in the original geometry, and 2 would result in a model made entirely of the inclusion material. Nine analyses were completed with the fraction of inclusions ranging from approximately 1% to 98%. The AEH technique was used to compute the four unique elasticity constants for the homogenized elasticity tensor.

For each of the nine cases, the elasticity tensor was also calculated two other ways. The first was according to the rule of mixtures (ROM). An effective modulus of elasticity was calculated as $E_e = f_i E_i + f_m E_m$. An effective Poisson's ratio was calculated similarly, and these were combined to compute the entries in the elasticity tensor. The second set of entries was calculated in a similar fashion except that the inverse rule of mixtures (IROM) was used, $E_e = (f_i/E_i + f_m/E_m)^{-1}$.

Fig. 4(a) and (b) show the resulting elasticity tensor entries. The ROM values are higher than the AEH values, while the IROM values are lower than their AEH counterparts. This is the expected
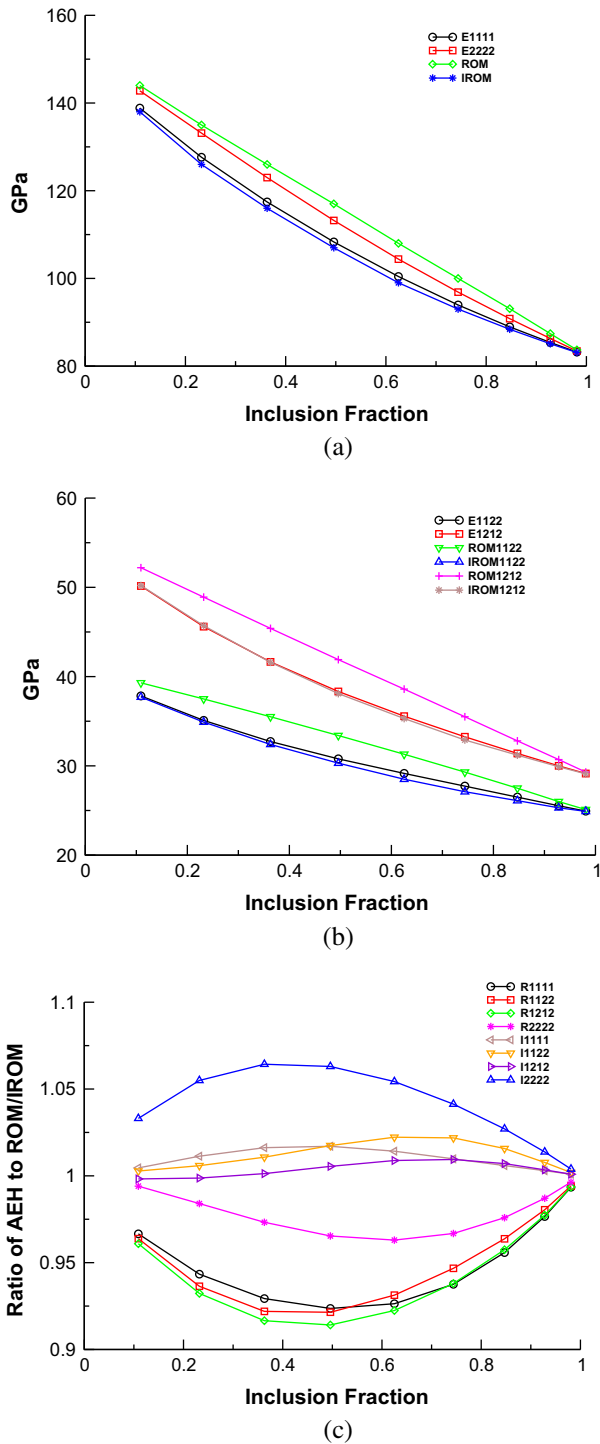
Fig. 4. In (a) and (b), AEH, rule of mixtures (ROM), and inverse rule of mixtures (IROM) elasticity tensor values. In (c), ratios of AEH to ROM and IROM values.

behavior. Fig. 4(c) shows the AEH values divided by the ROM and also the IROM values. This figure shows that there may be close to a 10% difference in AEH and ROM values.

Note that the elasticity constants do not vary considerably from ROM/IROM values when the fraction of inclusions is low. However, the differences increase with increasing fraction of inclusions up to ~0.5 inclusion fraction. With higher inclusion fractions, the ratios move toward 1, as expected. An analysis with different geometry or material properties would see different ratios, but the trends would remain the same.

For a given analysis, using AEH elasticity constants in place of volume averaged constants will lead to similar differences in computed stresses. That is, 5–10% differences in elasticity constants will result in ~5–10% differences in stresses. However, the AEH approach will produce anisotropic constants, whereas the volume averaged approach will only produce isotropic constants. Though not investigated here, the AEH approach can also provide a detailed local stress assessment, and these local stresses could differ by much more than 10%.

While no independent solution is available that would allow a measure of the error for this problem, the short fiber problem of Section 4 has independent solutions that match that computed by the AEH approach. If those solutions are taken as the correct solution, it is interesting to note that the ratio of the AEH solution to the ROM solution is 0.59. This indicates that the simplest approaches to considering the complete system, namely volume averaging the material constants, must be undertaken with caution. The AEH approach, however, is an extremely efficient approach that can be expected to provide more accurate results.

Despite the simplicity of this cladding/hydride model, it shows some of the potential of the AEH technique for investigating cladding behavior. Further enhancements might include a study of the effect of orientation on the overall response; the effect of a statistical variation in inclusion properties; behavioral changes given additional oxide inclusions; and the effect of inclusion shape and size.

6.2. Thermal conductivity of UO_2

In nuclear reactor fuel, fission gas atoms diffuse to grain boundaries and form grain boundary bubbles. As these bubbles grow, they significantly decrease the thermal conductivity of the fuel. In the following example, the effective thermal conductivity is calculated for various densities of bubbles on grain boundaries. The homogenized thermal conductivity is computed in two ways. In the so-called direct approach, the homogenized value is an applied flux times the length of the domain divided by the average change in temperature over that length. This direct calculation is accompanied by the AEH calculation of the thermal conductivity according to Eqs. (22) and (23).

Models with 5, 10, 15, and 20 bubbles on the grain boundary were analyzed. See Fig. 5. The thermal conductivity of the bubbles is dramatically lower than the thermal conductivity in the grains, leading to lower thermal conductivity with increasing number of bubbles. In addition, the thermal conductivity is reduced slightly from the bulk value to account for the grain boundary thermal resistance, or Kapitza resistance. The thermal conductivity value used in the bulk is 4.75 W/m/K, along the grain boundary is 3 W/m/K, and in the bubbles is 0.0056 W/m/K.

Fig. 6 shows the homogenized thermal conductivity in the x (horizontal) and y (vertical) directions for the direct and AEH approaches for each of the four models. It is clear that increasing numbers of bubbles does result in lower thermal conductivity.

One other detail is noteworthy. For the first three cases, the four homogenized values are similar. However, for the 20 bubble case, the thermal conductivity in the x direction as computed by the direct approach is noticeably lower than the other three values. The direct method is very sensitive to bubbles existing on the boundary where the flux is applied. Since the thermal conductivity is calculated from the average temperature on that side, if a bubble forms on the domain boundary, thus locally lowering the temperature, it can significantly affect the prediction. The AEH method is not sensitive to such local details.

Computing homogenized thermal conductivity using two-dimensional models will result in an overestimation of the drop in thermal conductivity with an increasing number of bubbles.
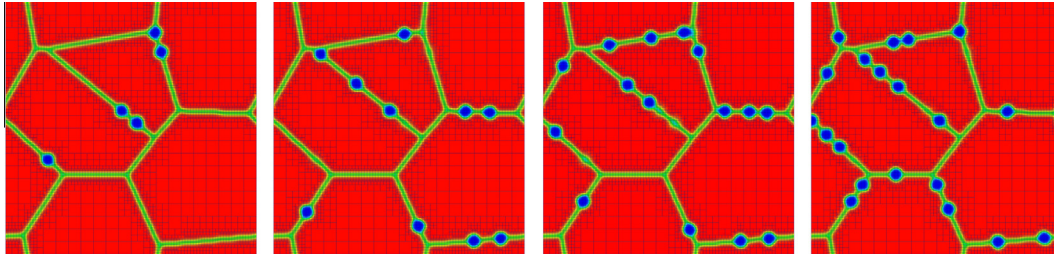
Fig. 5. Five, ten, fifteen, and twenty bubbles along the grain boundary for a 2D model in the *xy* plane.
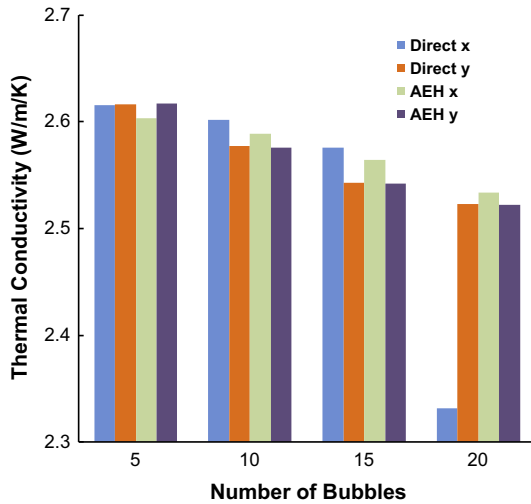

Fig. 6. Homogenized thermal conductivity for the direct and AEH methods in the *x* and *y* directions. The direct method gives a significantly lower thermal conductivity in the *x* direction for the case of 20 bubbles due to a bubble on the domain boundary.

However, the results of this analysis (namely that thermal conductivity drops with increasing bubbles and that the direct approach has a local sensitivity while the AEH approach does not) hold regardless of the dimension of the demonstration.

In summary, the AEH approach gives satisfactory results for this thermal conductivity analysis. It has a low computational overhead and is straightforward to implement. In addition, the technique has a consistent approach for thermal conductivity and elasticity homogenization.

7. Demonstration

In [11], MARMOT and BISON were coupled in a multiscale analysis. BISON computed macroscale temperature and neutron flux. These quantities were passed to MARMOT, which evolved the microstructure using the phase field method and computed the effective thermal conductivity of the microstructure. This mesoscale simulation tracked bubble nucleation and growth, and the thermal conductivity of the evolving microstructure was calculated using the direct method discussed above. The thermal conductivity was returned to BISON for its use at the macroscale. MARMOT ran at four points in a small rodlet, and the resulting thermal conductivity was interpolated throughout the fuel domain modeled by BISON.

Here, we again couple BISON/MARMOT for a demonstration of multiscale coupling. In this case, we analyze a single fuel pellet with three sets of six MARMOT calculations providing thermal conductivity according to the AEH approach. In this proof-of-concept calculation, each set of six MARMOT calculations is distributed from the pellet center to outer edge. One set is positioned near the top of the pellet, another at mid-pellet, and the last near the bottom of the pellet. The MARMOT calculations have static microstructures with various numbers of grain boundary bubbles.

In nuclear reactor fuel performance codes, the density of grain boundary bubbles is typically quantified using a grain boundary fractional coverage f_c, or the percentage of grain boundary covered by fission gas bubbles. The fission gas diffusion is a function of temperature, such that the grain boundaries near the hot center of the fuel have larger fractional coverage than those near the outer edge. To simulate this effect in this demonstration calculation, each of the MARMOT simulations receives a different temperature from BISON. In addition, each radial position simulation uses a different fractional coverage, with decreasing void fraction with increasing radius.

The fractional coverages for the six MARMOT simulations are taken from a separate calculation in BISON in which the fission gas release model [24] calculates the fractional coverage throughout the fuel pellet. For the six locations, the fractional coverages were $f_c = 0.31, 0.22, 0.13, 0.069, 0.036,$ and 0.011. This led to MARMOT models with 37, 26, 15, 8, 4, and 1 bubbles randomly distributed along the grain boundary. The microstructure with 15 bubbles is shown in Fig. 5.

This multiscale simulation gives results for the initial full-power solution. The orthotropic thermal conductivity is mapped from the MARMOT locations to BISON. The thermal conductivity in the radial direction is shown in Fig. 7(a). See Fig. 7(b) for the BISON temperature distribution.
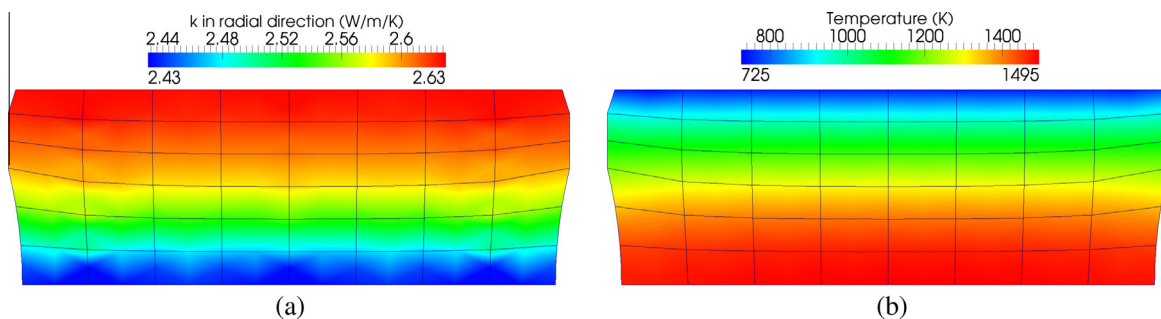

(a)

(b)

Fig. 7. Thermal conductivity in the radial direction in (a). Temperature distribution in (b).

The AEH method provides an accurate and efficient means of calculating the effective thermal conductivity that functions well for multiscale fuel performance calculations such as those outlined here. With further development, it will be possible to evolve the microstructure through time, including bubble growth, bubble migration, and grain growth. This will provide a changing thermal conductivity that is a function of local temperature and irradiation effects.

8. Conclusions

Asymptotic expansion homogenization has a strong history of development in the mathematical and engineering fields. It is applicable for homogenization of thermal conductivity, elasticity constants, and other quantities. It has a low computational expense (the same as steady state heat conduction or linear elasticity) and is straightforward to implement. It is thus a vehicle for enabling multiscale analysis.

The AEH approach has been implemented in BISON/MAR-MOT where it has been shown to solve standard benchmark problems accurately. It has also been shown to give good results without overly fine meshes.

Possible nuclear fuel analysis applications of the technique include estimating the mechanical response of cladding tubes that have hydride inclusions and computing homogenized thermal conductivity in nuclear fuel with grain boundary fission gas bubbles.

Future work with AEH in BISON/MARMOT will focus on better understanding the mesoscale to macroscale coupling in nuclear fuel and cladding. It is anticipated that the technique will prove to be a robust and accurate way to inform macroscale models of lower length-scale evolution.

Acknowledgements

References

[1] J.K. Fink, J. Nucl Mater. 279 (1) (2000) 1–18.
[2] P.G. Lucuta, Hj. Matzke, I.J. Hastings, J. Nucl. Mater. 232 (2–3) (1996) 166–180.
[3] J.M. Guedes, N. Kikuchi, Comput. Methods Appl. Mech. Eng. 83 (2) (1990) 143–198.
[4] Somnath Ghosh, Kyunghoon Lee, Suresh Moorthy, Int. J. Solids Struct. 32 (1) (1995) 27–62.
[5] B. Hassani, E. Hinton, Comput. Struct. 69 (1998) 707–717.
[6] G. Laschet, M. Apel, Steel Res. Int. 81 (2010) 637–643.
[7] João A. Oliviera, Joaquim Pinho-da-Cruz, Filipe Teixeira-Dias. Advances in Composite Materials – Analysis of Natural and Man-Made Materials, chapter 23. InTech, 2011.
[8] L.Q. Chen, Annu. Rev. Mater. Res. 32 (2002) 113–140.
[9] André Zaoui, J. Eng. Mechan. 128 (8) (2002) 808–816.
[10] Mark Horstemeyer, Multiscale modeling: a review, in: J. Leszczynski, M.K. Shukla (Eds.), Practical Aspects of Computational Chemistry, Springer Science+Business Media, 2009, pp. 87–135.
[11] R.L. Williamson, J.D. Hales, S.R. Novascone, M.R. Tonks, D.R. Gaston, C.J. Permann, D. Andrs, R.C. Martineau, J. Nucl. Mater. 423 (2012) 149–163.
[12] M.R. Tonks, D. Gaston, P.C. Millett, D. Andrs, P. Talbot, Comp. Mat. Sci. 51 (1) (2012) 20–29.
[13] D. Gaston, C. Newman, G. Hansen, D. Lebrun-Grandié, Nucl. Eng. Des. 239 (2009) 1768–1778.
[14] D.A. Knoll, D.E. Keyes, J. Comput. Phys. 193 (2) (2004) 357–397.
[15] J.D. Hales, R.L. Williamson, S.R. Novascone, D.M. Perez, B.W. Spencer, G. Pastore, J. Nucl. Mater. 443 (2013) 531–543.
[16] Pavel Medvedev, Fuel performance modeling results for representative FCRD irradiation experiments: Projected deformation in the annular AFC-3A U-10Zr fuel pins and comparison to alternative designs. Technical Report INL/EXT-12-27183 Revision 1, Idaho National Laboratory, 2012.
[17] N.N. Carlson, C. Unal, J.D. Galloway, Formulation of the constituent distribution model implemented into the BISON framework for the analysis of performance of metallic fuels with some initial simulation results. Technical Report LA-UR-13-26824, Los Alamos National Laboratory, 2013.
[18] J.D. Hales, M.R. Tonks, F.N. Gleicher, B.W. Spencer, S.R. Novascone, R.L. Williamson, G. Pastore, D.M. Perez, Ann. Nucl. Energy (2014). Accepted.
[19] Enrique Sanchez-Palencia, Homogenization of second order equations, in: Non-Homogeneous Media and Vibration Theory, Lecture Notes in Physics, volume 127, Springer, Berlin/Heidelberg, 1980, pp. 45–83. 10.1007/3-540-10000-8_5.
[20] P.W. Chung, K.K. Tamma, R.R. Namburu, J. Thermophys. Heat Tr. 15 (2001) 10–17.
[21] Peter W. Chung, Kumar K. Tamma, Raju R. Namburu, Compos. Part A: Appl. Sci. Manuf. 32 (9) (2001) 1291–1301.
[22] Kyu-Tae Kim, Nucl. Eng. Technol. 42 (3) (2010) 249–258.
[23] Joe Rashid, Mark Rashid, Albert Machiels, Robert Dunham, A new material constitutive model for predicting cladding failure, in: Proceedings of Top Fuel 2009, Paris, France, September 6–10 2009.
[24] G. Pastore, L. Luzzi, V. Di Marcello, P. Van Uffelen, Nucl. Eng. Des. 256 (2013) 75–86.